Petroleum Sciences

The combination of acidizing and hydraulic fracturing for the stimulation of a tight gas reservoir in Minas Gerais

http://dx.doi.org/10.1590/0370-44672024780010

Humberto Oliveira[1,3]
https://orcid.org/0000-0002-9910-5827
Cláudio Lúcio Lopes Pinto[1,4]
https://orcid.org/0000-0001-9924-2824
Thaís de Oliveira Soares[1,5]
https://orcid.org/0009-0006-1868-043X
Alexandre Uhlein[1,6]
https://orcid.org/0000-0002-0768-608X
José Maria dos Santos Júnior[2,7]
https://orcid.org/0009-0000-9609-2533
Henrique Ribeiro[2,8]
https://orcid.org/0000-0002-8824-9120
Antonio Eduardo Clark Peres[1,9]
https://orcid.org/0000-0002-6257-9084

[1]Universidade Federal de Minas Gerais - UFMG, Escola de Engenharia, Departamento Engenharia de Minas, Belo Horizonte – Minas Gerais - Brasil.

[2]Universidade Federal de Itajubá – Unifei, Departamento de Engenharia Mecânica, Itajubá – Minas Gerais - Brasil.

E-mails: [3]humbertohall@hotmail.com, [4]cpinto@demin.ufmg.br, [5]thaisoares7@gmail.com, [6]auhlein@gmail.com, [7]junior_unifei@hotmail.com, [8]henriquetoby@yahoo.com.br, [9]aecperes@demet.ufmg.br

Abstract

The combination of acidizing and hydraulic fracturing, or proppant-acid fracturing, seems to be a very logical approach to achieve the maximum stimulated volume in tight gas reservoirs, since the acid solution can stimulate the deep microfracture network far beyond the main propped fracture. However, this hybrid stimulation method sparks concerns that acidizing can increase proppant embedment and decrease the propped fracture conductivity. To understand how acidizing may be responsible for reducing conductivity, this article initially delves into the analysis of microscopic images of carbonate and siltstone specimens associated with a low permeability or tight gas reservoir in the São Francisco basin, in Minas Gerais, a kind of reservoir which is becoming considerably more important in recent years due to energy transition initiatives. The microscopic analysis revealed that thin, well-defined layers emerged on the acidized surface of some of the studied specimens. Then additional nanoindentation and proppant embedment tests showed that these new layers are weaker compared to the original rock matrix and are ultimately responsible for fracture conductivity decline. The findings in this study serve as an important piece of information for reservoir stimulation professionals that may consider the combination of acid stimulation and hydraulic fracturing in tight gas formations.

Keywords: proppant-acid fracturing, proppant embedment, tight gas, fracture conductivity, energy transition.

1. Introduction

The idea of proppant-acid fracturing was patented in the last century by Cardwell *et al.* (1957), but the first of this hybrid stimulation technique has only been published in the last decade (Azevedo *et al.*, 2010; Smith *et al.*, 2018; Che *et al.*, 2018). Likewise, only recently, laboratory studies on proppant-acid fracturing have begun to appear in the scientific literature, highlighting here Zhang *et al.* (2018), Guo *et al.* (2019) and Chen *et al.* (2023).

The new laboratory study presented here is based on the comparison of mechanical properties between acidized and non-acidized specimens of carbonate and siltstone rocks. The rocks used in this study are associated with a low permeability reservoir containing dry natural gas from the Bambuí Group in the São Francisco Basin, in Minas Gerais. In the Bambuí Group (Figure 1), the siltstone from Lagoa do Jacaré formation and the carbonates from Sete Lagoas formation are considered the gas-generating rocks; the carbonates from the upper part of the Sete Lagoas Formation, represented by the biogenic carbonates known as stromatolites (Vieira *et al.*, 2007), are the reservoir rocks of the Bambuí Group (Avila *et al.*, 2020).

In the first phase of the study, microscopic analysis of the acidized surfaces revealed thin, well-defined layers resulting from acid attack. The stromatolite, the only rock in this study with a biogenic origin, did not produce new layers due to acid etching and the probable reasons are discussed later herein.

In the second phase of the study, the nanoindentation tests allowed to compare the rock mechanical properties of acidized and non-acidized specimens, followed by proppant embedment tests that allowed to evaluate the fracture conductivity decline in the acidized specimens.

Figure 1 - Section of the stratigraphic column of the Bambuí.
Group in the São Francisco basin. Carbonates from the upper part of the Sete Lagoas Formation, represented by the biogenic carbonates known as stromatolites, make up the main gas reservoir in the Bambuí Group (Ávila *et al.*, 2020).

Proppant embedment represents the main cause of fracture conductivity loss (Gao *et al.*, 2013) and the factors that have the greatest influence on proppant embedment are related to the characteristics of the formation (clay content, organic carbon content, porosity of formation, carbonate and quartz content) and the characteristic of the proppant (proppant type, size, and concentration) (Bandara *et al.*, 2019).

All the tests reported here were performed under ambient pressure and temperature conditions. It is assumed, however, that the results of this work, which are based on the reaction rate of hydrochloric acid (HCl) and calcium carbonate ($CaCO_3$), would still be valid for reservoir conditions where pressures and temperatures are generally higher. The reason for this assumption is the fact that temperature and pressure have opposite effects on the reaction rate of HCl and $CaCO_3$. While the effect of increasing temperature is to increase the reaction rate (Alkattan *et al.*, 1998), the effect of increasing pressure is to decrease it, even when gas bubbles resulting from the reaction between HCl and $CaCO_3$ are kept in solution (Mumallah, 1991).

2. Theory

2.1 Fracture conductivity

Fracture conductivity depends on the permeability of the proppant filling the interior of the fracture, and the width of the fracture according to Equation (1):

$$F_c = k_f \times w_f \tag{1}$$

in the equation above, F_c is the fracture conductivity, k_f is fracture permeability, or the proppant permeability, and w_f is the fracture width.

The permeability of the proppant can be measured experimentally, or it can be calculated from the empirical Carman-Kozeny equation, Equation(2), widely used to predict the permeability of random sphere packages (Sanematsu *et al.*, 2015).

$$k_f = \frac{d_p^2 \varnothing^3}{180\ (1 - \varnothing)^3} \tag{2}$$

where d_p is the median proppant diameter and ϕ is the porosity of the proppant package.

2.2 Nanoindentation

The theoretical basis of nanoindentation was stablished by Oliver and Pharr (1992), and generally this process can be carried out either on a constant loading rate (CLR) mode or on a constant strain rate (CSR) mode. The majority of nanoindentation studies in rocks are performed using the CLR mode, where the maximum load needs to be pre-determined and deeper indentation depths indicate inferior mechanical properties (Shi *et al*., 2020).

Figure 2 illustrates the nanoindentation process where the indentation depth (h_{max}) in Equation (3) corresponds to the vertical surface deflection at the perimeter of contact (h_s) plus the contact depth (h_c).

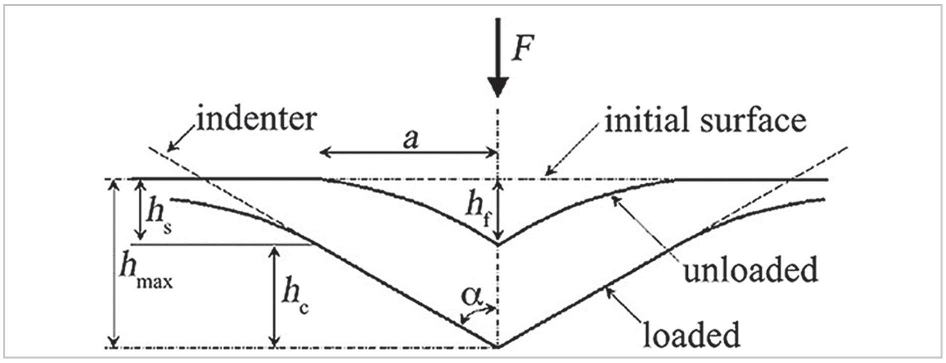

Figure 2 - Schematic cross-section of a nanoindentation process. Modified from Oliver and Pharr (1992).

$$h_{max} = h_s + h_c \quad (3)$$

Figure 3 illustrates the load vs. displacement curve which consists of three stages: loading, holding, and unloading.

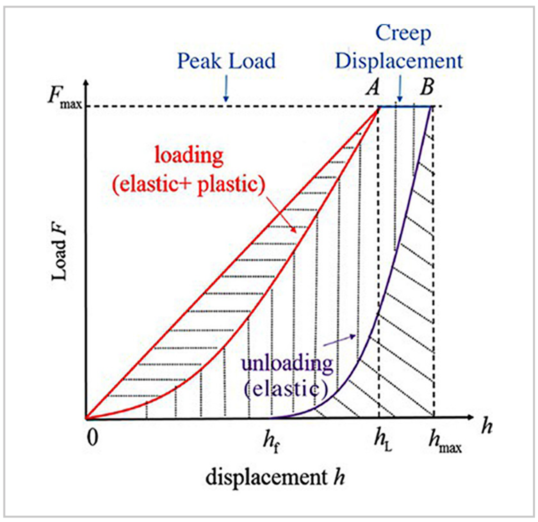

Figure 3 - Nanoindentation curve (Load vs. displacement). Modified from Shi *et al.* (2020).

The loading stage is a combination of elastic and plastic deformation, while the unloading stage consists of elastic (recovered) deformation.

The holding stage, also called creep displacement (Li *et al.,* 2019), is used to study creep behavior. According to Liu *et al.* (2018), as the creep time increases, Young's modulus and hardness decreases indicating that the sample´s surface becomes softer.

The unloading stage is used to calculate hardness (H) in Equation (4):

$$H = \frac{F_{max}}{A_C} / h_{max} \quad (4)$$

F_{max} is the peak load and A_c is the projected contact area of the indenter computed by Equation (5):

$$A_C = 24.5\, h_c^2 \quad (5)$$

h_c is the contact depth defined by Equation (6):

$$h_c = h_{max} - 0.75 \frac{F_{max}}{S} \quad (6)$$

h_{max} is the maximum indentation depth and S is the contact stiffness shown in Equation (7), calculated by the slope of the linear portion of the unloading curve (h_{max}):

$$S = \frac{dF}{dh} / h_{max} \tag{7}$$

where F is the load.

The reduced Young's modulus (E_r) can be calculated from Equation (8):

$$E_r = \frac{\sqrt{\pi S}}{2\beta\sqrt{A_c}} \tag{8}$$

β is a constant dependent on the geometry of the indenter (1.034 for a Berkovich indenter).

The Young´s modulus (E) can be calculated from Equation (9):

$$\frac{1}{E_r} = \frac{1 - v^2}{E} - \frac{1 - v_i^2}{E_i} \tag{9}$$

E_i is the Young's modulus and v_i is the Poisson's ratio of the diamond indenter (for a Berkovith indenter, E_i = 1141 GPa and v_i = 0.07), and v is the Poisson's ratio of the sample, usually taken from literature.

3. Methods and materials

3.1 X-ray fluorescence, x-ray diffraction and carbon phase analysis

X-ray fluorescence (XRF) was used for semi-quantitative chemical analysis while X-ray diffraction (XRD) was used for mineralogical composition analysis of the rock types in Figure 1. Carbon phases, i.e., organic, elemental carbon, and carbonate carbon, were determined by infrared absorption using a LECO carbon analyzer.

3.2 Preparation of samples for optical microscopy, scanning electron microscopy (SEM), and nanoindentation analysis

Sections for microscopy and nano indentation analysis were prepared from 56 mm diameter core samples containing a 6 mm diameter central hole.

During the acidizing procedure, the core samples were positioned vertically and 15% (w/w) HCl was injected in the central hole from the bottom, at a 15 mL/min rate, atmospheric pressure, and laboratory temperature (22° C), for 1 hour. In this dynamic test, the CO_2 bubbles continuously moved away from the walls in the central hole, not preventing the contact of the acid with the rock surface.

The cross-sections shown in Figure 4 were cut at a distance of 10 mm from the acid entry point. They show the results of acid dissolution in the central hole for the three different types of rocks. The reaction of carbonates (limestone & stromatolite) with HCl ($CaCO_3 + HCl \rightarrow CaCl_2 + CO_2 + H_2O$) showed the highest dissolution rates, especially in the stromatolite with a rock matrix rich in micropores (Figure 7), effectively exposing more of the rock surface to the acid. The siltstone on the other hand, rich in silicates that do not react with HCl (Figure 8), showed only a bleached layer around the central hole, without any visible enlargement of the original diameter.

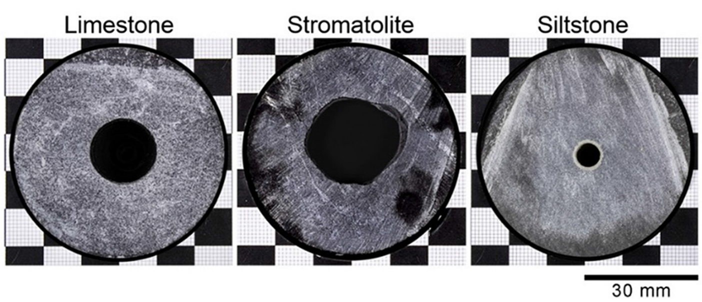

Figure 4 - Cross-sections of core samples after injection of 15% hydrochloric acid (HCl) into the 6 mm diameter central hole. Note the difference in reaction rate between the carbonate samples (limestone and stromatolite) and the siltstone.

After acid etching, the samples in Figure 4 were impregnated with a low-viscosity epoxy resin introduced while the samples were under a vacuum. After the vacuum impregnation, pressure via an inert gas was applied to force the epoxy into small pores. Blue is usually the color chosen to stain the resin, to facilitate the observation of pores under the optical microscope.

3.3 Sample preparation for proppant embedment tests

The specimens for the proppant embedment tests were prepared from larger core samples with 98 mm in diameter and 40 mm in height. Part of the specimens had one of the surfaces acidized by immersion in 300 ml of 15% HCl solution for a period of 1 hour (Figure 5).

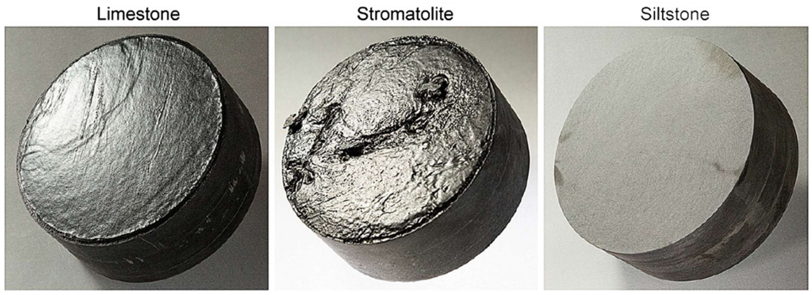

Figure 5 - Acidized core samples prepared for proppant embedment tests. Note the different textures between the stromatolite with the highest dissolution rate, and the siltstone with the lowest dissolution rate.

4. Results and discussion

4.1. XRF, XRD and carbon phase analysis

The chemical, mineralogical and carbon phase analysis for the rocks associated with the tight gas reservoir are presented in Tables 1, 2 and 3 respectively.

Among the minerals in Table 2, only calcite has a strong reaction with HCl. Between the clay minerals, muscovite and chamosite, the chamosite is more soluble in HCl and it can effectively be dissolved in HCl solutions with a concentration > 1N (3.64 % HCl) (Hu *et al.*, 2022). The quartz and albite (feldspar) are essentially insoluble in HCl.

In Table 3, it can be seen that the stromatolite has a higher content of elemental carbon compared to the limestone. Even though these concentrations apparently are very small, they could theoretically influence the deposition of a calcite layer as further explained in section 4.3.

Table 1 - Chemical analysis (XRF).

Rock	LOI Total $CaCO_3$	Direct Combustion Total Sulfur (%)	X-Ray Fluorescence (%)				
			Al_2O_3	CaO	Cr_2O_3	Fe_2O_3	K_2O
Siltstone	2.96	0.04	12.37	1.4	<0.01	5.13	2.66
Stromatolite	40.44	0.01	0.34	49.91	<0.01	0.12	0.14
Limestone	43.20	0.03	<0.1	55.68	<0.01	0.1	0.01
Rock	X-Ray Fluorescence (%)						
	MgO	MnO	Na_2O	P_2O_5	SiO_2	TiO_2	-
Siltstone	2.08	0.08	2.88	0.21	69.26	0.84	-
Stromatolite	0.38	0.01	<0.1	0.04	8.51	0.01	-
Limestone	0.12	0.01	<0.1	0.12	0.66	0.01	-

Table 2 - Mineralogical analysis (XRD).

Rock	X-Ray Diffraction (%)				
	Calcite ($CaCO_3$)	Quartz (SiO_2)	Muscovite ($KAl_2(Si_3AlO_{10})(OH)_2$)	Albite ($NaAlSi_3O_8$)	Chamosite ($(Fe^{2+};Mg;Fe^{3+})_5Al(Si_3Al)O_{10}(OH;O)_8$)
Siltstone	4.5	41.1	17.6	26.2	10.6
Stromatolite	91.5	8.5	-	-	-
Limestone	99.3	0.7	-	-	-

Table 3 - Carbon phase analysis.

Rock	Organic Carbon (%)	Elemental Carbon (%)	Carbonatic Carbon (%)
Siltstone	<0.05	0.06	<0.05
Stromatolite	<0.05	0.17	10.97
Limestone	<0.05	0.12	11.47

4.2 Optical Microscopy

Figure 6 shows optical microphotographs of thin sections (0.03 mm) extracted from the surface of the cross-sections in Figure 4. The blue resin that was applied to protect the internal walls of the acidized holes is clearly visible at the bottom of the pictures. The original rock matrix is labeled A, while the new layers resulting from acid etching are labeled B and C. Note the absence of neo layers in the stromatolite, and the blue resin penetrating the voids created by the acid reaction with calcite in the acid invasion zone in the siltstone.

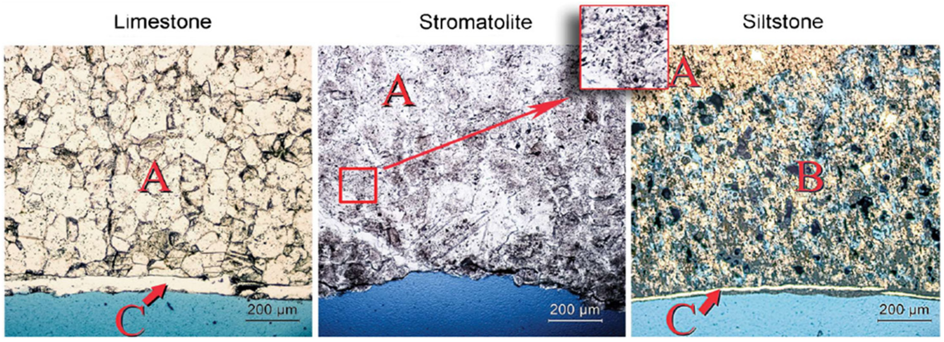

Figure 6 - Petrographic thin sections showing the original rock matrix (A) and the neo layers resulting from acid etching (B and C).

4.3 SEM images

Figure 7 shows SEM images from the surface of the cross-sections in Figure 4. The blue resin applied in the central holes appears dark on the left side of each picture. SEMs achieve higher resolution revealing finer details when compared to optical microscopes, because they rely on a focused beam of electrons that interacts with the sample and have a much shorter wavelength than visible light.

With SEM it is possible to clearly see the crystals forming neo layer C, in the limestone and in the siltstone, and the micropores in the matrix of the stromatolite.

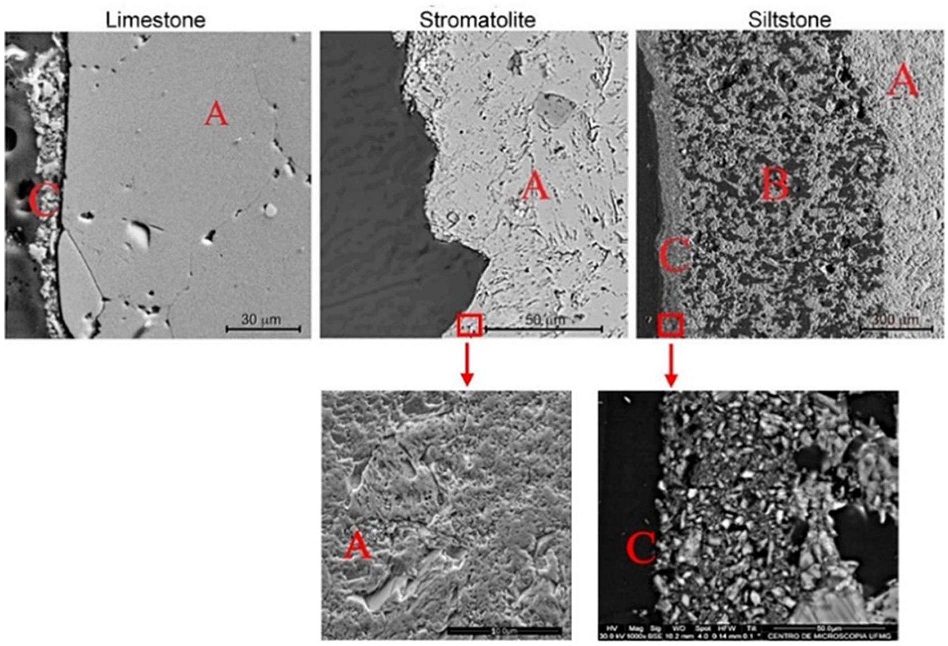

Figure 7 - SEM images from the surfaces of the cross-sections in Figure 4.
Notice the micropores in the stromatolite and the crystals from neo layer C in the siltstone.

4.4 SEM-energy dispersive X-Ray spectroscopy (EDS)

The energy dispersive spectrum (EDS) detector of the SEM provided a chemical mapping of the cross-sections in Figure 7. It is possible to observe in Figure 8 that calcite, indicated by the chemical element Ca, is the only mineral present in neo layer C in the limestone; but in the siltstone, in neo layer C, calcite is together with muscovite (K), albite (Na), chamosite (Fe) and quartz (Si). It seems that the fine grains of muscovite, albite, chamosite, and quartz, that were held together by calcite in the matrix of the siltstone, got lose during the solubilization of calcite in the acid invasion zone B and were cemented together in zone C during the recrystallization process of calcite, at the end of the acidizing procedure. In summary, these observations indicate that the outer neo layer C is the result of the recrystallization of calcite, both in the limestone and in the siltstone.

In Zone B, the acid invasion zone in the siltstone, calcite (Ca) was completely removed, while the other minerals from the matrix A remained intact; there is no observable transition for the chemical elements Si, Al, Na, K, Fe and Mg, from zone B to A, indicating that quartz, muscovite, albite and even chamosite were not removed from the original rock matrix. In summary, zone B is a residual neo layer resulting from the solubilization of calcite alone.

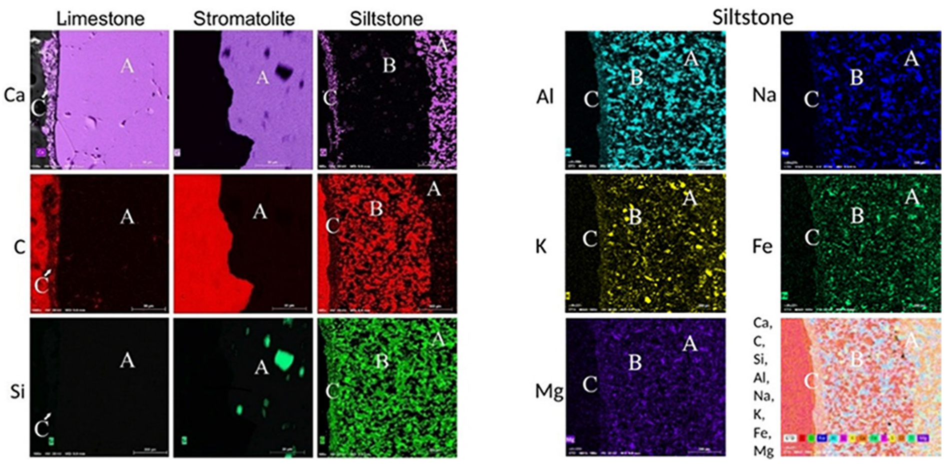

Figure 8 - Left - EDS mapping for Ca (calcite), Si (quartz), and C (blue resin).
Right – EDS mapping for K (muscovite), Na (albite), Fe & Mg (chamosite), and Al (muscovite, albite, chamosite) in the siltstone.

The reason for the absence of a recrystallization neo layer (C) in the stromatolite, whose presence would be expected based on a mineralogical composition similar to the limestone, is probably twofold. Primarily the high dissolution rate observed in the stromatolite creates a turbulent solid-liquid interface, disturbing the fixation of recrystallized calcite at the top of the matrix A. Then, along with the turbulent interface, comes the higher elemental carbon content of the stromatolite (Table 3). Carbon nano particles are efficient calcium carbonate scale inhibitors at concentrations as low as 10 mg/L in aqueous solutions. They change the crystal form of the precipitated calcite, making its adherence to surfaces a difficult task. However, any concentration values below the 10 mg/L threshold sharply reduce the efficiency of carbon as calcite scale inhibitors. (Wan *et al.*, 2019). Therefore, small variations in the low carbon concentration range could have a significant influence on the presence of a calcite deposition neo layer.

4.5 Nanoindentation tests

Nanoindentation tests were carried out using a Berkovich indenter at a constant loading rate of 70 µN/s and a maximum load of 700 µN maintained at peak load for 10 s. The indentation points were located at the vertices of a 50 x 50 µm square grid.

The nanoindentation was performed on the petrographic thin sections from Fig. 6, and the neo layers (B and C) were tested separately from the original matrix (A). The neo layers presented deeper indentation depths compared to the original rock matrices, confirming weaker mechanical properties, as is observable in Figure 9 and Figure 10. The stromatolite was the only rock that did not present neo layers resulting from the acidizing process (Figure 11).

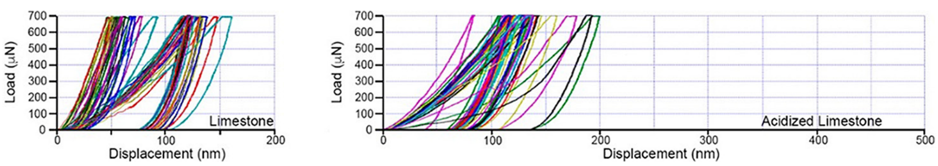

Figure 9 - Load-depth curves for the limestone and its respective acidized surface (neo layer C).

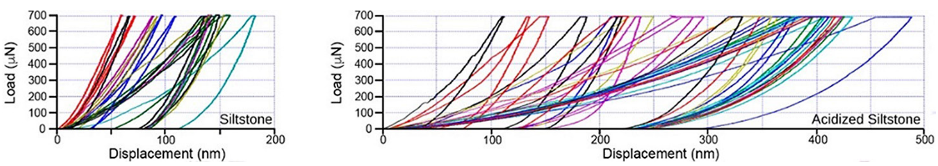

Figure 10 - Load-depth curves for the siltstone and its respective acidized surface (neo layers B and C).

The siltstone was the type of rock most affected by the acid attack. The indentation curves for neo layers B and C (Figure 9) reached depths up to 500 nm and showed large creep displacements (plateaus). As the plateaus on top of the indentation curves increase, the Young´s (elasticity) modulus and hardness decreases indicating that the samples become softer (Liu *et al.*, 2018).

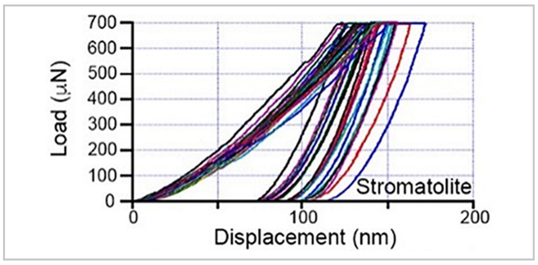

Figure 11 - Load-depth curves for the stromatolite (Zone A in Figure 6).
Unlike the previous two cases, the stromatolite did not present neo layers resulting from the acid etching.

A box and whisker plot for hardness, indentation depths, and Young´s modulus resulting from the nanoindentation curves is presented in Figure 12.

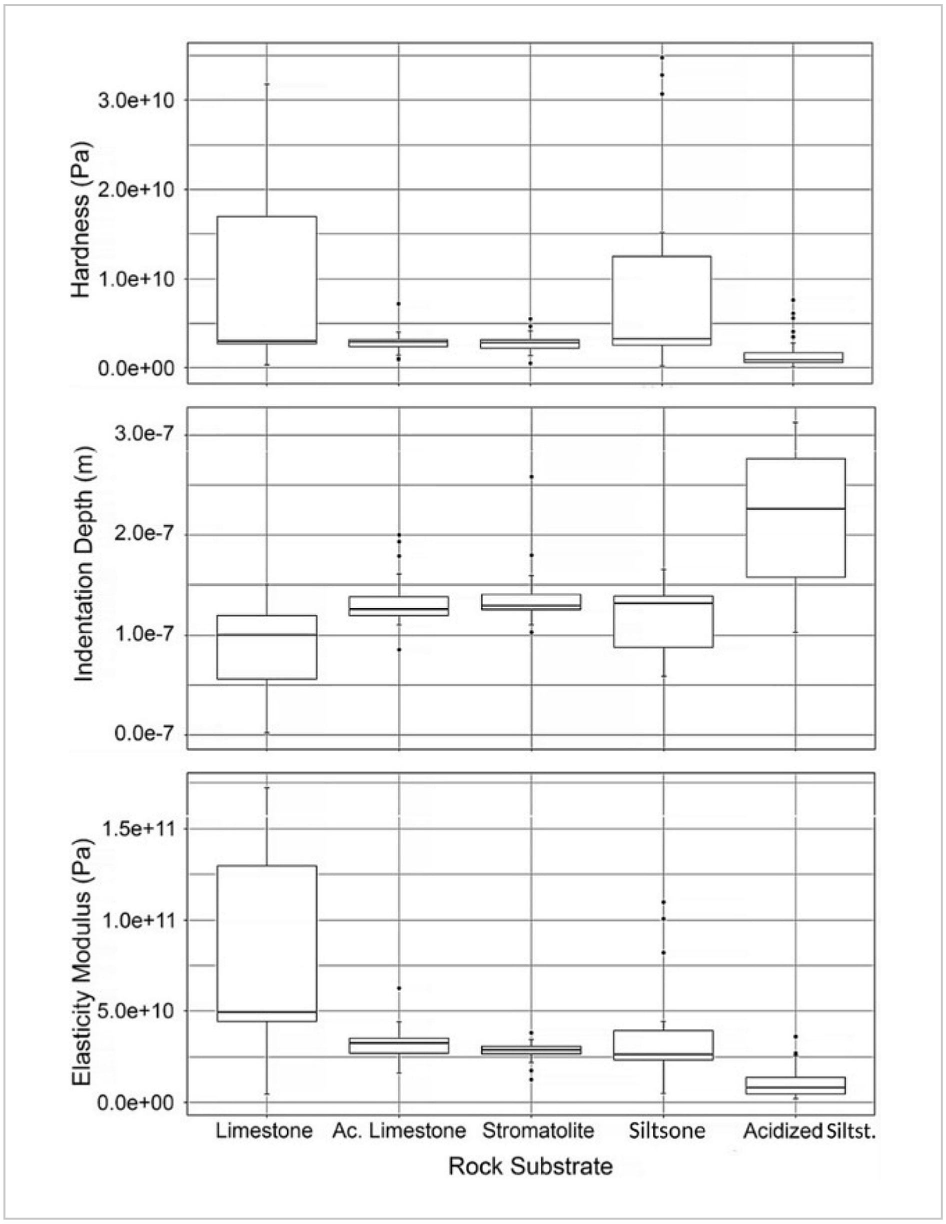

Figure 12 - Box and whisker plot for hardness, indentation depths, and
Young´s (elasticity) modulus analysis from the nanoindentation curves from Figure 9 to Figure 11.

4.6 Proppant Embedment and fracture conductivity decline

The proppant embedment tests used SinterBall Bauxite (HSP) 20/40 (425-850 μm), at 10.00 Kg/m^2 (2.0 lb/ft^2) proppant concentration, for 8 hours under a pressure of 40 MPa (5800 psi). The proppant was provided free of charge by Mineração Curimbaba.

Proppant embedment values were determined by measuring the total axial compression of pairs of non-acidized and acidized rock waffles (Figure 5), compressing the proppant package between them, and comparing to the total axial compression of non-acidized pairs without proppant.

In Figure 13, it is possible to observe that the acidized siltstone presented the highest values for proppant embedment. This was in fact already expected, as the acidized siltstone presented the thickest set of neo layers. The acidized stromatolite without neo layers, on the other hand, presented the lowest value for proppant embedment among the acidized specimens. Finally, the acidized limestone, containing only the recrystallization neo layer C, an intermediate situation between the acidized siltstone and the acidized stromatolite, also presented an intermediate value for the proppant embedment.

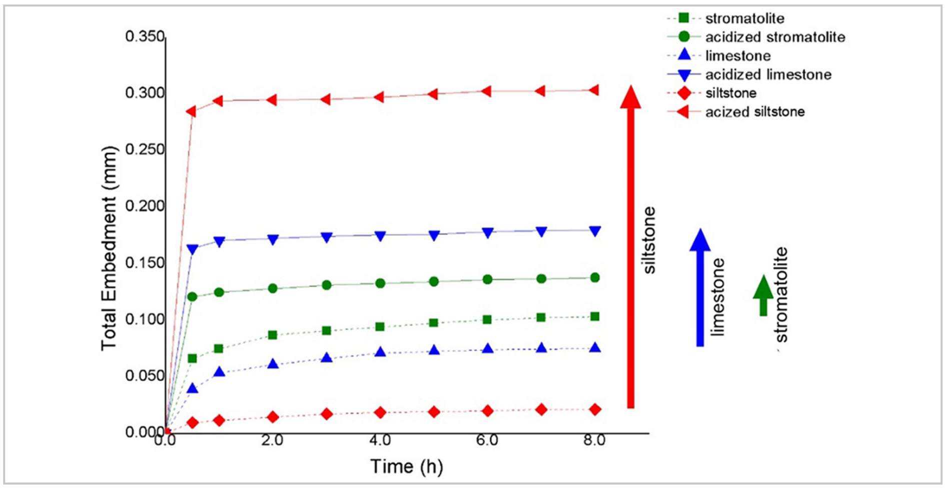

Figure 13 - Total proppant embedment results for pairs of acidized and non-acidized specimens.

The decline in fracture conductivity for the acidized siltstone, limestone and stromatolite is presented in Table 4. It was calculated with Equation 1 using the proppant embedment results in Figure 13 (at 8h) together with the proppant permeability information from the proppant manufacturer's website (www.curimbaba.com.br). The Siltstone presented the highest value of fracture conductivity decline and the stromatolite presented a minimum value of less than 1%. The small decline in the stromatolite was not caused by the presence of neo layers, but rather by the crushing of the rough surface texture resulting from its high dissolution rate.

Table 4 - Fracture conductivity decline in acidized samples.

Rock	Proppant Data from Curimbaba: Permeability: 4,368 x 106 md (2% KCl) at 40 MPa, 2.0 lb/ft^2. Proppant package width: 13.99 x 10^{-3} ft				
	Total Embdement (ft)	Total Embedment w/ Acid (ft)	Conductivity (md-ft)	Conductivity w/ Acid. (md-ft)	Frac. Conductivity Decline (%)
Siltstone	0.070 x 10^{-3}	0.996 x 10^{-3}	6081	5676	- 6.65
Stromatolite	0.339 x 10^{-3}	0.452 x 10^{-3}	5964	5914	- 0.83
Limestone	0.246 x 10^{-3}	0.590 x 10^{-3}	6004	5854	- 2.50

5. Conclusions

The combination of acidizing and hydraulic fracturing can increase the stimulated reservoir volume in oil and gas reservoirs, since the acid solution can reach and stimulate the microfracture network far beyond the main propped fracture, reaching distances within the reservoir horizon that the proppant is not able to do.

The microscopic and nanoindentation analysis of rocks associated with a tight gas reservoir in the Bambuí Group, of the São Francisco Basin, in Minas Gerais, revealed that the reservoir rock, the stromatolite, in contrast with the gas-generating rocks, does not produce weak neo layers resulting from the acid attack which are responsible for the increase in proppant embedment and loss of fracture conductivity. Conveniently the gas-generating rocks, that bound the reservoir rock, would be ultimately unaffected by hybrid fracturing as they have lost its gas to the reservoir rock over millions of years.

Therefore, proppant-acid fracturing, a hybrid stimulation, is the technique of choice recommended for the tight gas reservoirs in the Bambuí Group and those analogue to it.

References

ALKATTAN, M. *et al*. An experimental study of calcite and limestone dissolution rates as a function of ph from -1 to 3 and temperature from 25 to 80 degrees c. ***Chemical Geology***, 151, 199-214, 1998. DOI:10.1016/ S0009-2541(98)00080-1.

AVILA, R. *et al*. ***Nota técnica*** n° 16/2020/sdb/anp-RJ: estudo realizado pela equipe da SAG para o subcomitê II REATE (programa de revitalização da atividade de exploração e produção de petróleo e gás natural em áreas terrestres), 2020. DOI:10.13140/RG.2.2.33384.70404.

AZEVEDO, *et al*. Challenges faced to execute hydraulic fracturing in Brazilian pre-salt wells. *In*: US ROCK MECHANICS

SYMPOSIUM, 44, US-Canada, 2010. Rock Mechanics Symposium, American Rock Mechanics Association.

BANDARA, K. *et al*. Improved understanding of proppant embedment behavior under reservoir conditions: a review study. ***Powder Technology,*** 2019.

BORTOLON NETO, L. *et al*. Conductivity and performance of hydraulic fractures partially filled with compressible proppant packages. ***International Journal of Rock Mechanics and Mining Sciences*** 74, 1-9, 2015.

CARDWELL, P. H. *et al*. ***Well treatment.*** US Patent 2,802,531, 1957.

CHE, M. *et al*. ***Propped fracturing in deep naturally fractured tight carbonate reservoirs,*** 2018. DOI:10.2118/191712-18RPTC-MS.

CHEN, D. *et al*. A permeability model for the hydraulic fracture filled with proppant packages under combined effect of compaction and embedment. ***Journal of Petroleum Science and Engineering*** 149, 428-435, 2017.

CHEN, X. *et al*. Hydraulic, acid, and proppant-carrying acid fracturing stimulation of volcanic reservoirs in Sichuan basin, China: an experimental study. ***Petrol. Science and Technology*** 41,731-749, 2023. DOI: 10.180/10916466.2022.2070207.

CURIMBABA. ***Data sheet técnico SinterBall bauxite (HSP).*** Curimbaba, 18 Apr. 2018. Disponível em: https://www.curimbaba.com.br/admin/media/uploads/produtosItens/c-a-sinterball-bauxite-bt430091-port-curimbaba.pdf. Acesso em: 21 jun. 2024.

GAO, Y.; LV, Y.; WANG, M.; LI, K. New mathematical models for calculating the proppant embedment and conductivity. *In*: IPTC - INTERNATIONAL PETROLEUM TECHNOLOGY CONFERENCE, European Association of Geoscientists & Engineers. p. Cp-350, 2013.

GUO, J. *et al*. Comprehensive study of fracture flow characteristic and feasibility of hybrid volume stimulation technique in tight fractured carbonate gas reservoir. ***Journal of Petroleum Science and Engineering*** 174, 362-373, 2019.

HU, B. *et al*. The effects of hydrochloric acid pretreatment on differ-ent types of clay minerals. ***Minerals*** 12, 1167, 2022. DOI: 10.3390/min12091167.

LI, C. *et al*. Indentation creep behavior of Fe-based amorphous coatings fabricated by high velocity oxy-fuel. ***Journal of Non-Crystalline Solids,*** 503, p. 62-68, 2019.

LIU, K. *et al*. Application of nanoindentation to characterize creep behavior of oil shales. ***Journal of Petroleum Science and Engineering*** 167, 729-736, 2018.

MUMALLAH. Factors influencing the reaction rate of hydrochloric acid and carbonate rock. SPE - INTERNATIONAL CONFERENCE ON OILFIELD CHEMISTRY, 1991. DOI:10.2118/21036-MS. sPE-21036-MS.

OLIVER, W. C.; PHARR, G. M. An improved technique for determining hardness and elastic modulus using load and displacement sensing in- dentation experiments. ***Journal of Materials Research*** 7, 1564-1583, 1992.

SANEMATSU, P. *et al*. Image-based stokes flow modeling in bulk prop- pant packages and propped fractures under high loading stresses. ***Journal of Petroleum Science and Engineering*** 135, 391-402, 2015.

SHI, X. *et al*. Application of nanoindentation technology for characterizing the mechanical properties of shale before and after supercritical CO_2 fluid treatment. Journal of CO_2 Utilization 37, 158-172, 2020.

SMITH, M. B. *et al*. Simulation, design, and application of acid + proppant stimulation in a carbonate reservoir. *In*: SPE - INTERNATIONAL HYDRAULIC FRACTURING TECHNOLOGY CONFERENCE AND EXHIBITION, Society of Petroleum Engineers. p. 1-16, 2018.

VIEIRA, L. C. *et al*. A formação Sete Lagoas em sua área-tipo: fácies, estratigrafia e sistemas deposicionais. ***Revista Brasileira de Geociências*** 37, 1-14, 2007.

WAN, C. *et al*. Effect of carbon nanoparticles on the crystallization of calcium carbonate in aqueous solution. ***Nanomaterials*** (Basel). 1, v.9, n. 2, p. 179, Feb. 2019. DOI: 10.3390/nano9020179. PMID: 30717114; PMCID: PMC6409635.

ZHANG, L. *et al*. A new method to improve long-term fracture conductivity in acid fracturing under high closure stress. ***Journal of Petroleum Science and Engineering*** 171, 760-770, 2018.

Received: 12 February 2024 - Accepted: 30 June 2025.

Authors' contributions

Humberto Oliveira (Corresponding author): *conceptualization (lead): data curation (lead), formal analysis (equal), investigation (lead), methodology (lead), project administration (lead), supervision (lead), validation (lead), visualization (lead), writing - original draft (lead), writing - review & editing (lead)*; **Cláudio Lúcio Lopes Pinto:** *conceptualization (equal): data curation (equal), formal analysis (lead), funding acquisition (equal), investigation (equal), methodology (equal), project administration (supporting), resources (equal), supervision (equal), validation (equal), visualization (equal), writing - review & editing (equal);* **Thaís de Oliveira Soares:** *data curation (equal), formal analysis (equal), supervision (equal), writing - review & editing (equal);* **Alexandre Uhlein:** *investigation (equal), validation (equal);* **José Maria dos Santos Júnior:** *validation (equal);* **Enrique Rey Estrada:** *validation (equal);* **Henrique Ribeiro:** *validation (equal);* **Antonio Eduardo Clark Peres***: project administration (lead), resources (lead), validation (equal).*

Funding information

There are no funders to report for this submission.

Conflict of interests

The authors declare that there is no conflict of interest.

Data availability

The authors state that this manuscript is based on the Doctorate's Thesis of Humberto Almeida Oliveira, entitled "Aplicação combinada de fraturamento hidraúlico e acidificação para estimulação de depósitos de gás não convencionais da Bacia do São Francisco," presented in 2023 at the Federal University of Minas Gerais, in the Graduate Program in Mining Engineering (DeMin, UFMG), with all data available at the following link: http://hdl.handle.net/1843/54824.

Associate Editor

Ricardo Cabral de Azevedo